Light-induced optical and nanostructural changes of Si gratings

ESTER ABRAM[1,2,*] [ID] AND PAUL PLANKEN[2,1] [ID]

[1]*Advanced Research Center for Nanolithography (ARCNL), Science Park 106, 1098 XG Amsterdam, The Netherlands*
[2]*Van der Waals-Zeeman Institute, University of Amsterdam, Science Park 904, 1098 XH Amsterdam, The Netherlands*
*e.abram@arcnl.nl

Abstract: In nanolithography, optical diffraction from gratings etched into the scribe lanes of semiconductor devices is used for wafer alignment. As these gratings become increasingly smaller, achieving sufficiently strong diffraction signals requires higher light fluences, increasing the risk of optical damage. This study explores light-induced optical and structural changes in flat silicon and gratings etched in silicon when exposed to single femtosecond laser pulses. We find that the fluence thresholds for all observed damage mechanisms are 10–50% lower in gratings compared to flat silicon. Here, the fluence thresholds for the onset of optical change and crater formation are approximately 91 mJ/cm^2 and 816 mJ/cm^2, respectively. For certain gratings, these thresholds drop to below approximately 40 mJ/cm^2 and 400 mJ/cm^2. We attribute this to local field enhancements caused by the grating topography. Using near-field Rigorous Coupled-Wave Analysis (RCWA), we calculated absorbed power density profiles to establish a correlation between damage fluence thresholds and the local absorbed power density. While the method provides damage threshold estimates in a rather time-efficient manner, we found only a moderate correlation between the calculated and experimental threshold fluences. Careful analysis of our measurements shows that the observed deviations in relative pump-induced reflection changes in gratings, compared to flat silicon, are primarily due to grating line deformation, the onset of which can serve as an early warning for catastrophic damage. At high fluences, deformations become larger, even giving rise to grating line inversion, where lines become valleys and valleys become lines. Our findings offer insights into predicting and mitigating light-induced damage in silicon gratings, which is relevant to semiconductor device manufacturing.

1. Introduction

In semiconductor device manufacturing, integrated circuits (ICs) are being made which consist of hundreds of different layers containing complex patterns [1]. For each lithography step, the wafer needs to be positioned with a very high accuracy. For this, alignment markers, often small gratings, are etched into the scribe lanes between the dies on the wafer. Light diffracted by these markers is used to measure the wafer position. To save wafer real estate, these alignment gratings are becoming smaller and smaller [2,3]. This forces the illuminated area to decrease in size too. To keep the amount of diffracted light and, thus, the signal-to-noise-ratio the same, an increase in incident optical fluence is required. Unfortunately, this also heightens the risk of light-induced damage. In the context of semiconductor device manufacturing, any permanent material or optical alteration is undesirable. Whereas the effect of material [4–6], wavelength [7–9], pulse duration [10,11], thickness [12,13] and surface topography [14–16] on light-induced damage has been studied extensively in the past, this has mostly been done on relatively flat surfaces.

Therefore, little is known about the effects of high optical fluences on the alignment gratings used in semiconductor device manufacturing.

Here we present experimental results from exposing six silicon gratings with varying pitches and duty-cycles, as well as a flat silicon sample, to single laser pulses at optical fluences above and below the threshold for catastrophic damage. Our findings show similarities with previous research on flat aluminum and ruthenium layers [6,17], in that optical changes occur below the ablation threshold fluence. These changes are attributed to single-shot melting and resolidification processes. Once the material surpasses its melting temperature, the grating lines start to deform and, at higher fluence, show line-valley inversion, where lines become valleys and vice versa. Our results confirm that the onset of optical changes coincides with the onset of structural deformation. They demonstrate that the fluence thresholds for all observed damage mechanisms are ≈10–50% lower in gratings compared to that of a flat silicon surface. These findings suggest that localized field enhancements, induced by the topography of the gratings, play a significant role in determining damage thresholds. This is reasonably well supported by Forward Diffraction Modelling using Rigorous Coupled-Wave Analysis (RCWA) [18], used to numerically solve Maxwell's equations, from which the damage threshold scaling with respect to the flat silicon surface is estimated. While this method is useful as a first step to estimate damage thresholds, we observed only a moderate correlation between the calculated and experimentally obtained threshold fluence values. This suggests that more advanced calculations that include heat diffusion, and possibly hydrodynamical models, nonlinear absorption effects in silicon, and other time-dependent effects, are needed for improved accuracy.

2. Experimental details

2.1. Sample overview

In this research, seven different samples have been studied: Flat bulk Si and six gratings etched in Si, each having different dimensions. The patterns were fabricated by ASML using a Baseliner Matched Machine Overlay mask [19] made by IMEC. First, a resist was deposited onto the silicon wafer, then developed and etched with a target depth of 80 nm. In practice, the resulting etch depth was closer to 70 nm. After etching, the resist was removed. No additional layers were present on the wafer, except for the native silicon oxide layer, which has a thickness of approximately 2.1 nm. An overview of the dimensions of all structures is given in Table 1. Table 2 lists relevant properties of Si and SiO_2. Since little is known about light-induced damage on grating structures, the samples are exposed by single-shot high intensity pulses only. This simplifies the analysis and is an important first step in increasing our general understanding of the optical and morphological changes that are induced by the light.

2.2. Setup

The pump-probe setup used for the experiments is shown schematically in Fig. 1 and is explained in more detail in [6]. Here, 45 fs laser pulses with a central wavelength of 800 nm are generated by a multi-pass Ti:Sapphire amplifier system at a 1 kHz repetition rate. Hereafter, the laser beam is split into a weak 800 nm probe beam and a strong 400 nm pump beam created by second harmonic generation in a Beta Barium Borate (BBO) crystal. The probe illuminates the sample under an angle of ≈10° with respect to the normal of the sample surface with the original repetition rate of 1 kHz. The fluence of the pump beam can be varied by rotating a $\lambda/2$-plate, placed before the BBO crystal. Next, a pulse picker system, formed by a 10% duty-cycle chopper and a galvo mirror, selects a single pump-pulse. The pump-pulse illuminates the sample at near-normal incidence. The probe and pump are focused onto the sample to ≈15 and ≈75 μm FWHM spot sizes respectively, while maintaining their original Gaussian beam profiles. The geometry of the beams and the sample are schematically shown in Fig. 1. In some cases, an

Table 1. Overview of the used Si samples. The pitch and duty-cycle design values, and the cross section of a single unit cell of each grating as obtained using atomic force microscopy are shown. The black scale bars have a length of 100 nm and all gratings have a ≈70 nm height.

Pitch (nm)	Duty-cycle (%)[a]	Cross section[b]
Flat	N/A	
430	23.2	
430	34.8	
460	50	
600[c]	50	
950	50	
980	50	

[a]The duty-cycle is defined as the ratio of valley width and grating pitch.

[b]The left slope appears to be less steep than the right. This is not an AFM artefact but is inherent to all gratings due to the etching process.

[c]There is a slight misprint in the 600 nm pitch grating: a small dent is observed at the left side of the facet following the left slope, which is apparent throughout the entire grating. However, this has a negligible effect on its optical response.

Table 2. Optical and thermal mechanical properties of silicon and silicon oxide

	Si	SiO$_2$
$n + ik$ @ 400 nm	$5.631716 + 0.285821i$[a]	1.744466[b]
$n + ik$ @ 800 nm	$3.679123 + 0.004060i$[a]	1.730794[b]
T_m (K)	1687[c]	
Thickness (nm)	Bulk	2.1[d] (native oxide)
k_0 @ 300 K (W m^{-1} K^{-1})	124.0[c]	
C_i @ 300 K (10^6 J m^{-3} K^{-1})	1.63[c]	

[a]Ref. [20, pp. 555-569]
[b]Ref. [21]
[c]Ref. [22, pp. 12-80]
[d]Obtained by ellipsometry

additional $\lambda/2$-plate before the focusing lens of the pump is used to rotate its original polarization by 90°.

Before each measurement series, a Gentec-EO Beamage-4M beam profiler is placed at the sample position where the pump and probe beam spatially overlap, to measure the pump and probe beam spatial profiles. Furthermore, a Coherent thermopile power sensor is placed in the pump beam path after the last mirror before the focusing lens. This is to calibrate the reference (switchable-gain Si) photodetector in order to convert the detector signal into a pump fluence.

A variety of different gratings is etched into each die of a silicon wafer. The grating lines have an amplitude of ≈70 nm, and each individual grating has dimensions of 2×2 mm. Therefore, as each pump shot has to illuminate a pristine, undamaged site, only a limited number of pump shots can illuminate each grating. As the pump has a FWHM of 75 μm on the sample, the spacing between pump shots is chosen to be 200 μm. Therefore, single pump pulses hit each grating in
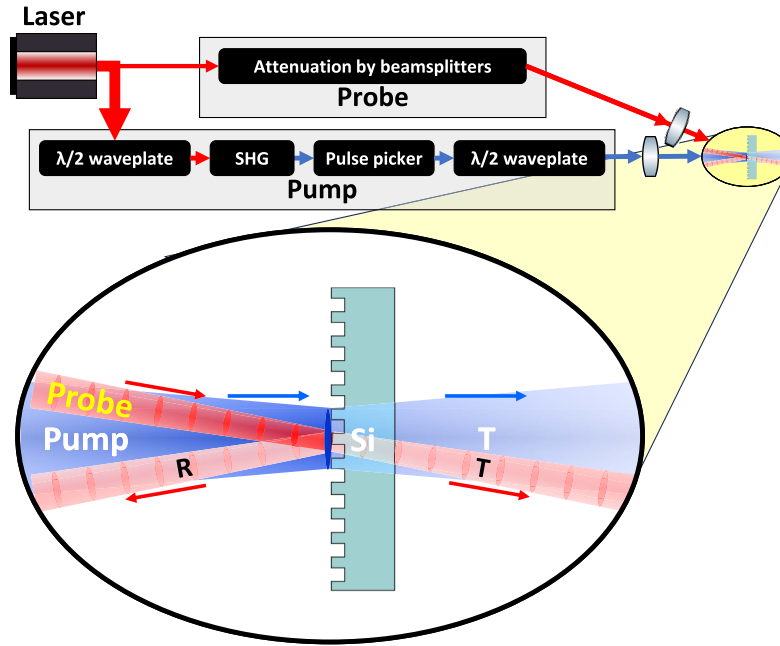
Fig. 1. Schematic of the experimental setup. The 45 fs, 800 nm laser output is split into a strong pump and a weak probe beam. The pump beam passes a Beta Barium Borate (BBO) crystal to frequency-double it to a 400 nm wavelength (SHG). The pulse-picking system selects single pulses. The pump pulse energy can be varied by rotating the $\lambda/2$-plate, which is placed before the BBO crystal. If a different polarization of the pump-beam is desired, an additional $\lambda/2$-plate is placed before the pump focusing lens that rotates the pump beam by 90°. R and T indicate the reflected and transmitted pump and probe beams. A detailed description of the entire setup can be found in [6].

a 8×9 grid. Each subsequent pump shot has a slightly higher fluence until half of the grid is covered. This illumination sequence is then repeated to check reproducibility, until the entire grid is filled. Here, the fluence ranges from well below any measurable morphological or optical change, to above the ablation threshold, where material is rapidly removed.

The experiments are repeated for different polarizations of the pump and probe beam relative to the grating lines. In total four different polarization combinations are used, where each set was performed on a new die. The polarization sets are schematically shown in Fig. 2.

At each illuminated site, before pump excitation, the 800 nm reflectivity R_{pre}, is obtained by measuring the probe reflection and a reference signal using photodetectors. R_{pre} is averaged over a thousand shots, giving $\bar{R}_{\text{pre}}$, which improves the signal-to-noise-ratio (SNR). The same is done for the thousand probe shots measured well after pump excitation (≥ 1 ms), when all transient effects have disappeared, giving the average $\bar{R}_{\text{post}}$. The relative difference between $\bar{R}_{\text{pre}}$ and $\bar{R}_{\text{post}}$ is the *relative reflection change* ΔR:

$$\Delta R(F) = \frac{\bar{R}_{\text{post}}(F) - \bar{R}_{\text{pre}}}{\bar{R}_{\text{pre}}}. \tag{1}$$

These values for ΔR depend on the pump fluence F and are obtained for all samples, and are presented in subsection 3.1. Because we divide all measured signals by a reference signal that scales with the incoming pulse energy, and because of the averaging over ≈ 1000 shots to obtain $\bar{R}_{\text{pre/post}}$ (see [6]), the error in ΔR around $\Delta R \approx 0$, almost only depends on
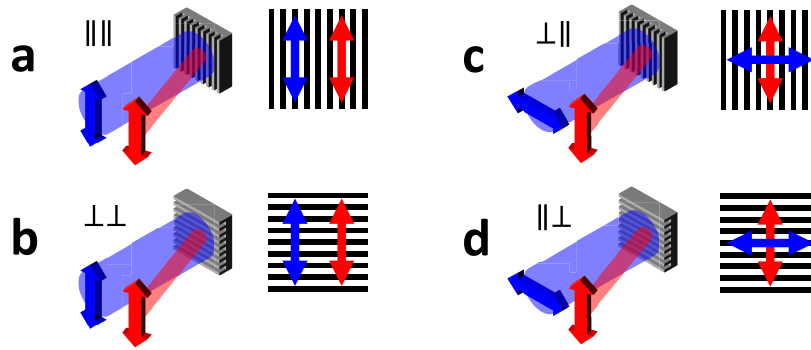
Fig. 2. Schematic drawing of the four polarization sets. For all samples, full pump-fluence-dependent scans have been obtained for all shown polarization sets. This resulted in 28 measurement series. We only used ∥ (parallel) and ⊥ (perpendicular) polarization of the pump and probe light with respect to the grating lines. Here we inspected ∥∥, ⊥⊥, ⊥∥ and ∥⊥ polarization where the first character denotes the polarization of the pump and the second that of the probe beam with respect to the grating lines. Since ∥∥ is the default polarization of the setup, the ⊥∥ and ∥⊥ polarizations have been made by transmitting the pump beam through a $\lambda/2$ waveplate. Additionally, the samples have been rotated by 90° around the normal of the sample surface to obtain the ⊥⊥ and ∥⊥ configurations.

environmental (temperature and humidity) and alignment (beam pointing and mechanical vibrations) uncertainties. We established an upper bound for the measurement uncertainty of ΔR in the pre-ablation regime to be 0.4%. Note that in the higher fluence regimes, the variation in ΔR is larger due to the smaller spot size of the probe and the randomness in the shape of the deformed Si grating lines and surface, and due to a randomness in the spatial distribution of debris.

2.3. Post-processing

After each measurement series, the sample is taken out of the laser setup for inspection of the illuminated sites. Each sample containing 72 illuminated sites is inspected by Bright-field (BF) and Dark-field (DF) microscopy. Hereafter, a Helios Nanolab 600 scanning electron microscope (SEM) is used to study possible morphological changes. Selected sites are inspected further with a Bruker Dimension Icon atomic force microscope (AFM).

Various damage mechanisms were observed across all samples, each bounded by a contour that defines where the local fluence equals the threshold for that damage mechanism. Given the elliptical Gaussian beam profile, the boundaries of each damage mechanism manifest themselves as concentric ellipses. To quantitatively analyze these ellipses, optical microscopy images were processed using OpenCV [23] and a RANSAC algorithm [24], enabling the precise fitting of ellipses corresponding to different damage mechanisms. For a Gaussian beam profile, the area A of each fitted ellipse scales linearly with $\ln(F_0)$. By performing a linear regression of A against $\ln(F_0)$ for each damage mechanism, we obtain regression lines that intersect $A = 0$ at the fluence threshold F_{th}. This approach, known as the Liu-analysis (see section I of Supplement 1), provides an accurate determination of the damage thresholds for all observed mechanisms. The probabilistic nature of the creation of damage is not very strong, as the damage threshold fluences were quite similar when the experiment was repeated. Further support for this is given by our Liu-analysis across all samples, which consistently shows that A scales linearly with $\ln(F_0)$. This linear relationship indicates that the damage thresholds are governed by a well-defined threshold fluence, and less by probabilistic effects.

3. Results and discussion

3.1. Optical response

3.1.1. In situ

In Fig. 3(a) we show the relative reflection change induced by a single 400 nm pump pulse on a flat silicon surface, as a function of peak fluence F_0. This measurement will be used as a reference to compare the gratings with. For low fluences, F_0 is too weak to induce an optical change ($\Delta R \approx 0$). However, above a certain fluence $F_\uparrow$, there is a steep ΔR increase. For further increasing fluences, ΔR starts to decrease (around $\Delta R \approx 30\%$) near the ablation threshold, and will eventually become negative. A somewhat similar behavior is observed for all gratings in this study (Fig. 3(b)–3(g)). However, next to similarities, there are also some differences. Although all gratings display a positive ΔR increase in the low fluence regime, the fluences where this occurs ($F_\uparrow$) are slightly (10-30%) lower than that for the flat silicon sample. Additionally, for $\perp$-polarized pump light, *two* local $\Delta R(F)$ maxima are present in some gratings. In the relatively high fluence regime, the fluence threshold values for ablation and crater formation (F_{abl} and F_{crater}), depend heavily on pump polarization and grating parameters.

As was previously shown for aluminum and ruthenium [6,17], the probe reflectivity can change due to single-shot melting and resolidification. There the grain structure (size and crystal orientation) changes, changing the electron mean free path, and therefore the effective refractive index of the metal. However, this is different for the silicon, which in the pristine state is monocrystalline. Nevertheless, melting and resolidification can change the single crystal into a polycrystalline [25,26] or amorphous structure [27–29], increasing the reflectivity up to 30-40% around 800 nm [25]. Additionally, local melting of the silicon will also result in the deformation of the grating lines, which alters the specular reflection of the probe beam. Furthermore, light-induced heating of the material can also cause enhanced oxidation [30]. Crystal structure change, grating line deformation and enhanced oxidation will all influence the probe reflection and therefore ΔR. Unfortunately, their contributions to the total reflection changes cannot easily be separated in the measurements. However, it is known that the reflection spectra of amorphous Si and crystalline Si are different. We therefore decided to use a Filmetrics F40-UV Film Thickness Measurement microscope [31] to perform reflection spectroscopy on pristine, and on laser-illuminated Si, both in flat areas on the wafer containing the gratings used in the experiments. By comparing this with the known reflection spectra of amorphous and crystalline Si, we can at least make qualitative statements on the changes of the Si after illumination. The results are shown in Section 4 of Supplement 1.

3.1.2. Ex situ

The probe reflectivity (Fig. 3) versus fluence can be divided into different fluence regimes. For fluences below the onset of ablation, so before the rapid removal of material, $\Delta R(F)$ displays various 'jumps'. These sudden changes in $\Delta R(F)$, are also visible in the optical microscopy images. Here, brighter areas are visible which are bounded by a local fluence F_{th}, that can give rise to sudden jumps of ΔR or $\frac{\partial \Delta R}{\partial F}$.

Figure 4 shows optical bright-field (BF), dark-field (DF), and scanning electron microscopy (SEM) images of three damaged sites. Figure 4(a)–4(c) depict a flat silicon site exposed to a pump pulse with a fluence exceeding the crater formation threshold at its center. Figure 4(d)–4(f) and Fig. 4(g)–4(i) display the same types of images for a 950 nm pitch, 50% duty-cycle grating, illuminated with $\perp$-polarized and $\parallel$-polarized pump light respectively. In all cases, the local pump fluence at the center of the illuminated sites exceeded the crater formation threshold, resulting in multiple damage mechanisms manifesting themselves at varying distances from the illumination center as the local fluence decreases.
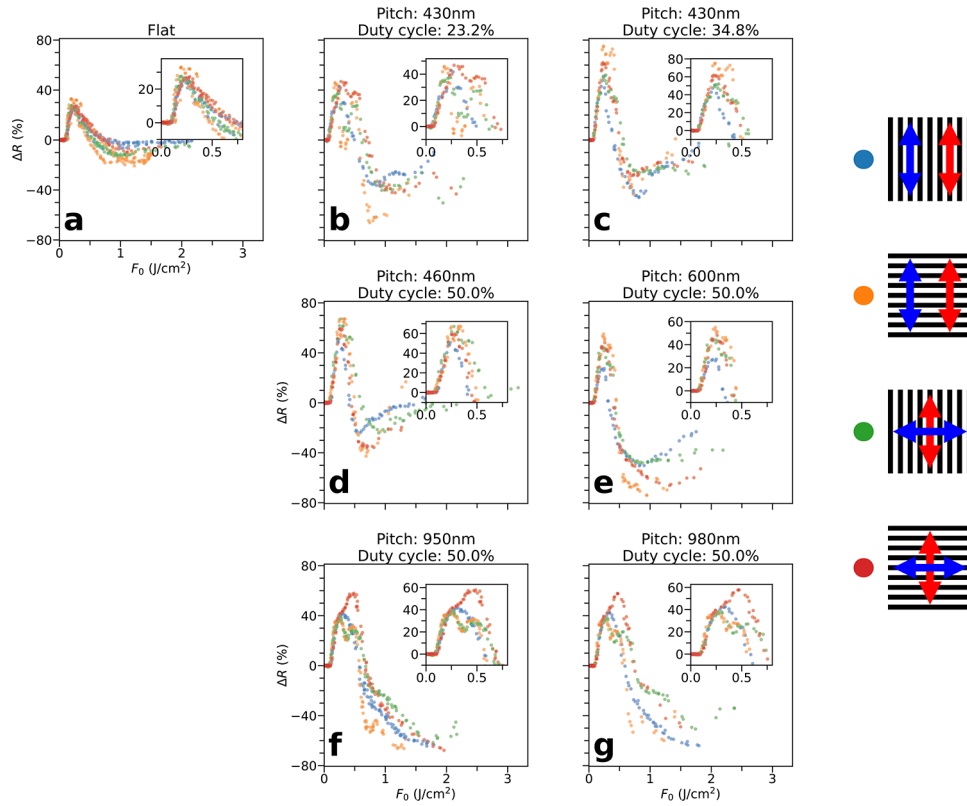
Fig. 3. Measured relative reflection change ΔR versus the peak pump-pulse fluence F_0 for the flat silicon surface (3(a)) and six silicon etched gratings (3(b)–3(g)). The colors indicate the pump and probe polarizations with respect to the grating lines, which is explained in more detail in Fig. 2. The uncertainty in ΔR of all data points in the $\Delta R \approx 0$ fluence regime is smaller than 0.4%. The stronger variation in the changes in the reflectivity seen for higher fluences are caused by variations in how the damage manifests itself. The error bars have been left out in the figures to avoid overcrowding them.

In Fig. 4(b), the dark-field image of the flat surface displays a single bright ring which represents the ablation edge. Outside this edge, but surprisingly, also inside the ablation edge, the surface is still relatively flat, and therefore appears dark in the image. Unlike the flat surface, the gratings scatter more strongly, making the dark-field image bright (Fig. 4(e) and 4(h)). Extracting the ablation edge is therefore less straightforward. Because of this, a set of edges is acquired by obtaining contours and fitting ellipses to the bright and dimmer rings visible in both the bright- and dark-field images. From the areas spanned by these ellipses, Liu-analysis is performed to obtain the corresponding fluence thresholds (see section I of Supplement 1). For each fluence threshold, the corresponding damage mechanism is obtained by inspection of additional SEM images. Liu-analysis has been performed for all samples and a list of fluence thresholds and corresponding damage mechanisms can be found in Table I in Supplement 1.
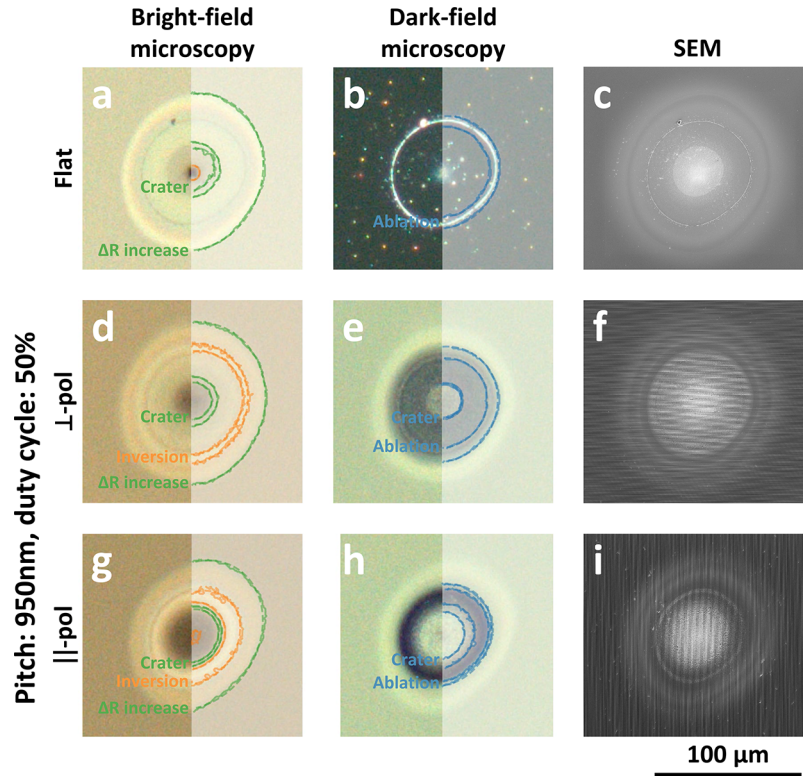
Fig. 4. Optical bright-field, dark-field and SEM images for three damaged sites: A flat silicon surface (4(a)–4(c)), and a 950 nm pitch, 50% duty-cycle grating illuminated with ⊥-polarization (4(d)–4(f)), and ‖-polarization (4(g)–4(i)). Because the local pump fluence exceeded the crater formation threshold in the center of all illuminated sites, all (lower fluence) damage mechanisms are observed when moving away from the illumination center, to lower local fluences. An ellipse fitting procedure applied to the damaged contours is compiled using an algorithm three times: Once using dark-field images, and twice using the bright-field images with two different contrast settings indicated by the blue, orange and green ellipses respectively. The corresponding damage mechanism is obtained by inspection of additional SEM images.

3.2. Fluence thresholds

First, the fluence threshold $F_\uparrow$ at which ΔR increases is determined. Since this is the lowest fluence where pump-induced (optical) changes form, it is very likely that only one process contributes to the optical change. Second, the grating lines deform, as is discussed in more detail in subsection 3.3. This deformation indicates that the melting threshold has been reached. This is still at relatively low fluences, but will affect the grating topography significantly. At F_{dark}, a dark shade is seen in the SEM images (Fig. 4). This is used to select the proper F_{dark} for the flat surface, since this dark shade is also visible on the flat surface where no grating line deformation can occur. Finally, the high-fluence damage thresholds F_{abl} and F_{crater} are determined. Here, material is ablated, where at F_{abl} material is removed superficially, and at F_{crater} a crater starts to form. F_{abl} and F_{crater} are distinguished by comparing the optical microscopy images with SEM images (see Fig. 4). In this high-fluence regime, some intriguing morphological changes are found in the gratings, such as line-valley inversion (see subsection 3.3).

Thresholds
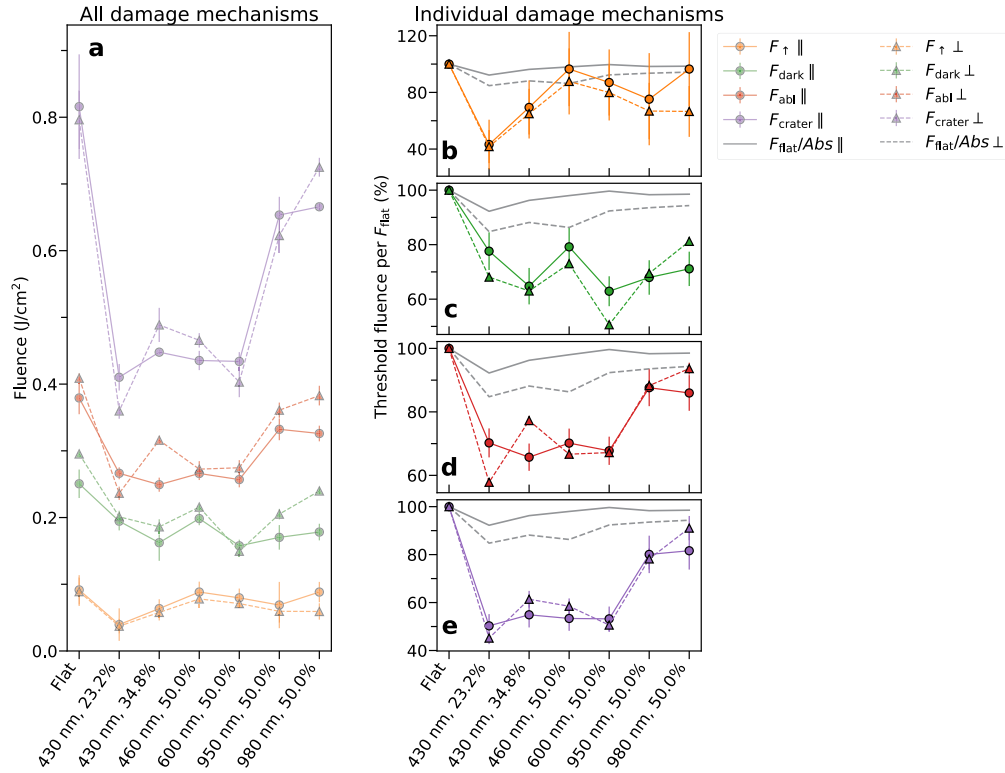
Fig. 5. Experimentally obtained fluence thresholds $F_\uparrow$ (orange), F_{dark} (green), F_{abl} (red) and F_{crater} (purple), shown together (5(a)), and individually (5(b)–5(e)), for the flat surface and gratings. The solid lines with round markers, and the dashed lines with triangular markers indicate parallel (∥) and perpendicular (⊥) pump polarization respectively. The lines connect the data points, and are included as a guide to the eye only. The black lines indicate $\frac{Abs_{\text{flat}}}{Abs}$, which is a line to show the inverse of the calculated absorbed fraction (*Abs*) scaled to the absorbed fraction of the flat surface. If the amount of total absorbed light defines the values of the damage threshold, the black lines should follow the $F_\uparrow$, F_{dark}, F_{abl} and F_{crater} data points (orange, green, red and purple), which they do not.

Figure 5(a) shows the threshold fluences $F_\uparrow$, F_{dark}, F_{abl} and F_{crater} found by Liu-analysis for the flat silicon surface and gratings. To compare the thresholds with that of the flat surface, the thresholds for each damage mechanism are shown separately in Fig. 5(b) to 5(e) and expressed as the fraction of their corresponding threshold value of the flat silicon surface. Additional SEM images are shown in Fig. 3(a) in Supplement 1. Since all samples only differ in surface topography, the difference in damage thresholds can only be attributed to the difference in grating parameters.

3.2.1. Total absorption

To learn more about the influence of the grating period and duty-cycle on the light-induced damage threshold, we determined how much light is absorbed in the gratings first. This is done by solving Maxwell's equations by performing Forward Diffraction Modelling using Rigorous Coupled-Wave Analysis (RCWA) [18]. First, the total absorbed fraction of the pump-pulse, $Abs = 1 - \sum_{n=0}^{N} R_n$ is computed where R_n is the nth order fraction of reflected/diffracted light.

Here we considered the first 50 diffracted orders (N=50). In Fig. 5(b) to 5(e), its inverse ($\frac{1}{Abs}$) is plotted for parallel (solid black line) and perpendicular (dashed black line) pump polarization for all gratings. To compare this with the obtained fluence thresholds, $\frac{1}{Abs}$ is multiplied by the calculated absorption for flat Si (Abs_{flat}). This is done so $\frac{1}{Abs} \cdot Abs_{\text{flat}}$ coalesces with the scaled measured fluence thresholds $\frac{F_x}{F_{x,\text{flat}}}$ for the flat Si in figure (5(b)–5(e)) (left most data point). Here x denotes the damage mechanism ('↑', 'dark', 'abl' or 'crater'). If the damage thresholds would depend only on the total absorption, the calculated values for $\frac{Abs_{\text{flat}}}{Abs}$ would follow the same trend as the measured $\frac{F_x}{F_{x,\text{flat}}}$ thresholds for the gratings. Because of the large spot size of the pump pulse ($\approx$75 μm), lateral heat diffusion at the center of illumination (the peak of the Gaussian beam profile) can be neglected. Therefore, F_x is the peak intensity fluence F_0, and is taken constant over the considered unit cell in our RCWA calculations. According to the calculated $\frac{1}{Abs}$ values, damage should occur at lower fluences in gratings in comparison with the flat surface, and parallel pump illumination should correspond to a lower threshold fluence. This is qualitatively in accordance with the measured fluence threshold behavior. However, the *measured* threshold fluence *variation* with grating parameters, compared to the *calculated* $\frac{1}{Abs}$, is significantly different. The difference between the measured threshold values is on average much greater than the total calculated absorption difference would suggest. This means that the total absorption is not the determining factor for the light-induced damage. For this reason, it is also useful to study how the light is locally absorbed in the grating, as it seems plausible that the grating parameters influence the *local* absorbed power density due to local field effects [32]. Therefore, near-field RCWA calculations are performed from which the local power density is calculated. Note that this is a first step towards understanding how surface topography will affect the light-induced damage threshold with respect to a flat surface. Our calculations do not take self-induced reflection/absorption changes during excitation with the 400 nm pump pulse into account. Including this is far from trivial [33] and has not been attempted here. Next to this, a further improvement of our prediction could be obtained by implementing phase transitions using two-temperature hydrodynamics [34,35] and heat diffusion effects. This would, in principle, result in a better physical description of the material.

3.2.2. Near-field calculations

From the calculated $\mathbf{E}(x, z)$ and $\mathbf{H}(x, z)$ fields (see also section III of Supplement 1), the time-averaged Poynting vector, $\langle \mathbf{S} \rangle$, is derived,

$$\langle \mathbf{S} \rangle(x, z) = \frac{1}{2} \text{Re}(\mathbf{E}(x, z) \times \mathbf{H}^*(x, z)), \tag{2a}$$

from which the local absorbed power density $\frac{du}{dt}$ equals

$$\frac{du}{dt}(x, z) = -\nabla \cdot \langle \mathbf{S} \rangle. \tag{2b}$$

In the case of linear absorption, the local absorbed power density $\frac{du}{dt}$ is proportional to the incident fluence F. Furthermore, the fluence is taken constant over the unit cell. In Fig. 6, $\frac{du}{dt}(x, z)$ is shown for all gratings illuminated with the same fluence F for both parallel and perpendicular polarization with respect to the grating lines. While for the flat surface, $\frac{du}{dt}$ falls of approximately exponentially when moving deeper into the material (Beer-Lambert law), concentrated 'hot-spots' emerge in the grating structures. The local absorbed power in those hot-spots can exceed the maximum value of $\frac{du}{dt}$ found in the flat samples by approximately a factor of 3, and strongly depends on grating parameters. Moreover, the grating parameters, as well as pump-polarization, determine the locations of the hot-spots. For parallel pump-polarization, the hot-spots are more localized at the grating line slopes, and for perpendicular pump polarization more towards the center of the lines.
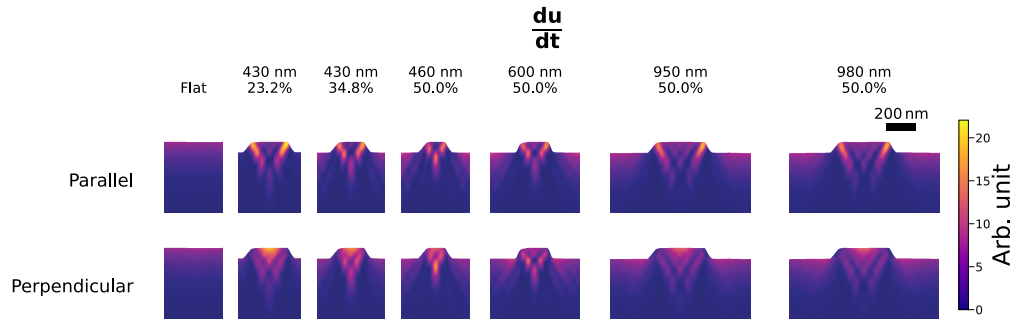
Fig. 6. The calculated absorbed local power density $\frac{du}{dt}(x,z)$ for all samples illuminated by the same incident fluence with a polarization parallel (top) and perpendicular (bottom) to the grating lines. The $\frac{du}{dt}(x,z)$ profiles are derived using Forward Diffraction Modelling using Rigorous Coupled-Wave Analysis (RCWA) [18] and linear absorption is assumed.

We can use the derived $\frac{du}{dt}(x,z)$ spatial profiles to calculate what the highest optical absorbed power density in the grating is and where this is reached. This can then be compared with that of a flat Si sample and with the measured damage thresholds to determine whether there is a correlation between the calculations and the experimentally obtained thresholds. This is done by calculating the mean value of $\frac{du}{dt}$ over an area A. While keeping the area size fixed, the exact shape of A is defined by maximizing the mean value of $\frac{du}{dt}$ bounded by A. More information can be found in section III of Supplement 1. By using these local power density maxima, and the experimentally obtained threshold fluences for the flat surface, we get the calculated fluence thresholds of the gratings (see section III.1 of Supplement 1). The correlation between the experimentally obtained F_{dark}, F_{abl} and F_{crater}, and the calculated values is stronger using the highest local absorbed power densities, compared to only considering the total integrated absorption. However, we still observe only a moderate correlation between the calculated and experimentally obtained values. In Fig. 6 in Supplement 1 we show that this also strongly depends on the chosen value for A. It seems likely, though, that localized field enhancements induced by the topography of the gratings play a significant role. From the $\frac{du}{dt}$ profiles in Fig. 6, it is clearly visible that these enhancements are experimentally lower in gratings with a larger pitch of 950 and 980 nm, which is in line with the experimentally observed higher damage thresholds. However, we only used the local absorbed power densities for the threshold determination, as obtained by RCWA. Therefore, only linear absorption is assumed. Incorporating heat diffusion [36] and, possibly, hydrodynamical models and nonlinear absorption effects in silicon [33], could significantly improve the model to estimate the fluence threshold of a patterned surface with respect to the threshold of the flat topography more quantitatively. This is, however, beyond the scope of this work.

3.3. Deformations

3.3.1. Height increase, flattening, and inversion

In the fluence range between the optical change threshold ($F_{\uparrow}$) and crater formation (F_{crater}), the grating lines undergo various deformations. Figure 7 illustrates these deformations with detailed SEM and AFM images using a 600 nm pitch, 50% duty-cycle grating illuminated by a single-shot ‖-polarized pump beam as an example. The SEM images (Fig. 7(a)) and cross-sectional profiles obtained via AFM (lines 1 to 6 in Fig. 7(b)) show the effect of the increasing local fluence (F) on deformation, when moving towards the center of the illumination spots. On the SEM images in Fig. 7(a), six lines are indicated by a number, which corresponds to the six cross sections of the lines as shown in the AFM images in Fig. 7(b). At relatively low fluences, the lines deform as

they increase in height and become less rectangular (lines 1 and 2). As the fluence increases, the lines broaden and decrease in height, eventually forming a small double ridge (line 3). Hereafter, the line flattens completely (line 4), and *inversion* starts to occur (line 5), where lines transform into valleys (also called spaces) and vice versa. Interestingly, the lines that emerge post-inversion can exceed the original grating line amplitude ($\approx$70 nm) while maintaining steep edges (line 6). Debris observed near the inversion onset (line 4) marks the ablation threshold (F_{abl}). As the local fluence approaches F_{crater}, the grating lines no longer have a fixed cross-section profile when taking cross sections of the same grating line in different locations along the line. This is due to irregular deformation along the grating line direction and is clearly visible in the irregular shape of the grating lines in the vertical direction in the lower right SEM image in Fig. 7(a).

3.3.2.   Grating parameters and polarization dependency

The deformation sequence described above is relatively consistent across all examined gratings. This is demonstrated in Fig. 3(a) in Supplement 1, where SEM line scans depict the evolution of deformations across the flat surface and for all six different gratings, each illuminated by $\perp$ or $\parallel$-polarized pump-pulses. While this general deformation pattern is observed across all samples, the specific progression depends on the grating parameters (pitch and duty-cycle) and pump polarization. Optical near-field calculations, discussed in subsection 3.2.2 and shown in Fig. 6, reveal that the local absorbed power density is differently distributed within the considered unit cells, depending on grating parameters and pump polarization. This will effect how the grating lines will deform. For $\parallel$-polarized pump illumination, the power is more concentrated at the grating line slopes, while for $\perp$-polarization, this is around the center of the lines. Larger pitches exhibit a more diffuse power absorption, especially under $\perp$-polarized light, which possibly explains the less pronounced inversion. This difference is visible when comparing the deformed line shapes of the 950 nm and 980 nm pitch gratings, compared to that of smaller pitches, as can be seen from the SEM line scans shown in Fig. 3(a) in Supplement 1. For the 430 nm/23.2%, 430 nm/34.8%, 950 nm/50% and 980 nm/50% samples, the shape of the deformed grating lines (for $F > F_{abl}$) differs substantially between $\parallel$ and $\perp$-polarization. These are the same samples that display the biggest change in local absorbed power density distribution (hot spots and distribution in Fig. 6) between the two considered polarizations as well.

### 3.3.3.   Reflection change affected by topography changes

Previous studies on flat aluminum and ruthenium layers [6,17] also show a reflectivity increase when exposed to single pump-pulse fluences below the ablation threshold. For the aluminum and ruthenium layers, this optical change is due to single-shot melting and resolidification, increasing the average grain size, leading to reflectivity increases between 0.1 and 5%. In silicon however, melting and resolidification changes the single crystal into a polycrystalline [25,26] or amorphous structure [27–29], which increases the reflectivity up to 30-40% around 800 nm [25]. By reaching this melting threshold, the resulting material flow can potentially cause the grating lines to deform. To further investigate the relationship between this topographical change and the optical reflection changes, RCWA far-field calculations were performed. Grating line deformation will directly change the diffraction efficiency, and thus change the measured reflection of the probe light. Therefore, we calculated the reflectivity of deformed grating lines that are exposed to a (local) fluence F, and compared this to the reflectivity of the unexposed geometry, resulting in a relative reflection change of the probe by only considering grating line deformation ΔR_{def} (Eq. (1)). In these calculations, it is thus assumed that the optical properties of the material itself have not changed. This is for sure incorrect but allows us to determine the effect of *only* a changing topography on the reflectivity. Each calculated ΔR_{def} value is obtained by making AFM scans of a few grating lines near the center of an illuminated site. From these, cross sections are obtained, and for each cross section the probe reflectivity is obtained by RCWA
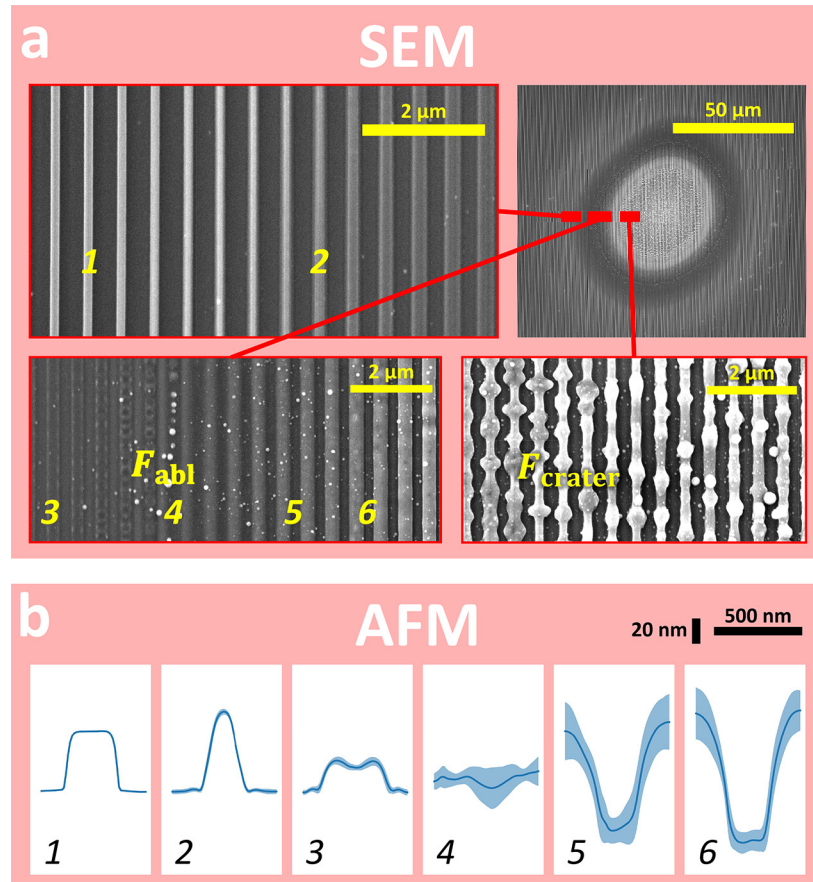
Fig. 7. Overview of grating line deformation of a site on a 600 nm pitch, 50% duty-cycle grating illuminated with a single ∥-polarized pump shot. (7(a)) SEM images, and (7(b)) cross sections measured by AFM. The local fluence F decreases when moving away from the illumination center. At the SEM images in (7(a)), the red rectangles mark the sections of which zoomed-in versions are also shown. The numbers *1-6* mark the approximate locations of the cross sections as obtained by AFM shown in (7(b)). The cross sections are derived from multiple 2D height maps obtained by AFM. Each height map covers 8×8 µm and consists of 1024 lines, where a variety of protocols such as row alignment, masking, and removing the polynomial background are implemented using Gwyddion software [37]. Hereafter, the median of these 2D height maps along the grating lines is taken as the cross-sectional height (blue line), and the standard deviation as the height uncertainty (blue shaded area). The black rectangles indicate the vertical and horizontal scale of the AFM cross sections. Note that the top-right image in (7(a)) may appear slightly different from Fig. 4(f) and 4(i). However, this discrepancy is solely due to differences in contrast settings applied during SEM image acquisition. In reality, they reveal the same damage characteristics.

far-field calculations. This is then compared with the calculated reflectivity of pristine grating lines, which results in a relative reflection change for each grating line cross section. Since each AFM scan spans several unit cells, averaging over the cross sections of all unit cells results in an average value for ΔR_{def}. This is then repeated for each illuminated site. The results of these calculated values of ΔR_{def} are shown in Fig. 8, together with the measured ΔR_{meas} versus fluence for a 980 nm/50% grating illuminated by single ∥ (Fig. 8(a)) or ⊥-polarized (Fig. 8(b)) pump pulses. The 980 nm/50% grating is considered here because of the significant difference of
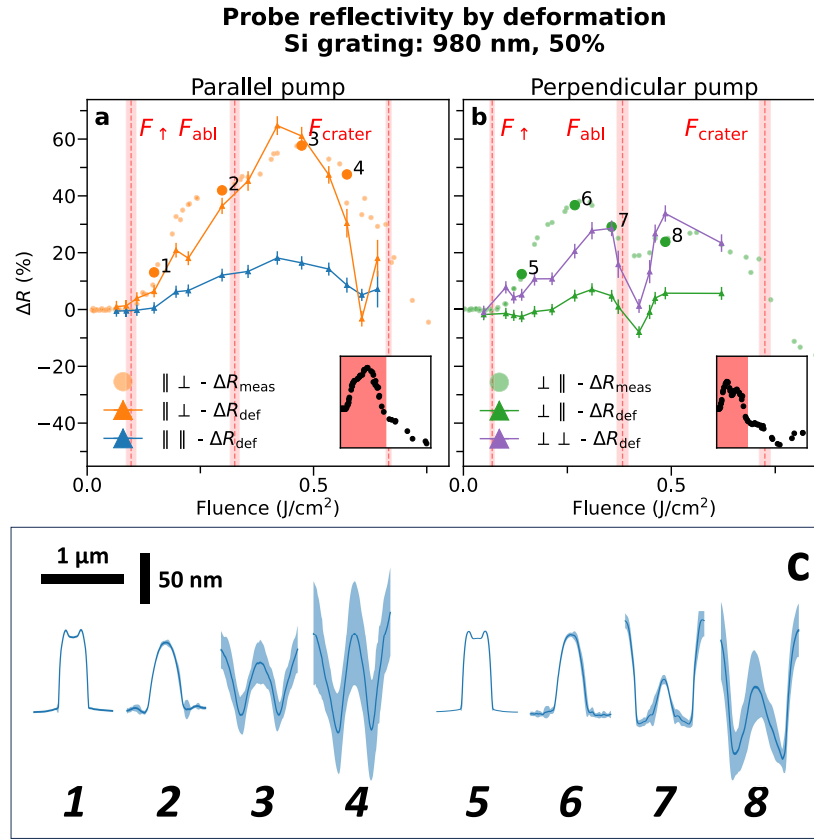
Fig. 8. (8(a)–8(b)) The measured and calculated relative reflection change of the probe pulses ΔR_{meas} and ΔR_{def} versus pump fluence F, induced by pump-pulses polarized parallel (8(a)) or perpendicular (8(b)) to the lines of a 980 nm, 50% duty-cycle silicon grating. The round markers correspond to the measured values of ΔR_{meas}, and the triangular ones to the calculated ΔR_{meas}. ΔR_{def} is derived by obtaining the cross sections of the deformed and pristine grating lines by AFM and by calculating the reflectivity using far-field RCWA [18]. For ΔR_{def}, both parallel and perpendicular polarizations are considered, and for ΔR_{meas} only one is measured: perpendicular at (8(a)) and parallel at (8(b)). The uncertainty in ΔR of all data points in the $\Delta R \approx 0$ fluence regime is smaller than 0.4%. The stronger variation in the changes in the reflectivity seen for higher fluences are caused by variations in how the damage manifests itself. For example, the "wobbliness" in the thickness of the grating lines has a random appearance, as does the distribution of debris at the surface at higher fluences. As the probe laser spot is smaller than the pump spot, it is more sensitive to these variations and the measurements thus display some variation in reflectivity. The error bars have been left out in the figures to avoid overcrowding them. *1-8* mark the data points that correspond to the deformed unit cell cross sections shown in (8(c)). The cross sections are derived from multiple 2D height scans obtained by AFM and processed as described in figure 7, using the median of the scans along the grating lines as the cross-sectional height (blue line), and the standard deviation as the height uncertainty (blue shaded area). The black rectangles indicate the vertical and horizontal scaling of the AFM cross sections.

the ΔR_{meas} curves between the two pump polarizations. As illustrated in Fig. 8(b), when the grating is illuminated by a perpendicularly polarized pump beam, the measured ΔR_{meas} exhibits

a characteristic double-peak behavior as the fluence increases. In contrast, this feature is absent when the grating is exposed to a parallel-polarized pump pulse, as shown in Fig. 8(a).

At fluences near F_{crater}, the grating lines exhibit significant (quasirandom) deformations along their length, which compromises the reliability of the calculated ΔR_{def} values. These deformations result in an ill-defined cross section of the unit cell as used as input for the RCWA code [18], as it relies on the assumption of a constant, smooth topography along the grating lines. Therefore, our analysis focuses on ΔR_{def} for fluences below F_{crater}. As shown in Fig. 8, The calculated ΔR_{def} begins to change around $F_\uparrow$, marking the onset of optical changes. This suggests that as optical changes occur, the grating lines start to deform, indicating that the material's melting temperature is reached at $F_\uparrow$. In the same figure where the measured ΔR_{meas} is shown, we have plotted the calculated ΔR_{def}, obtained by using the measured fluence dependent grating line cross-sections in the RCWA calculations. It reproduces the same key features as ΔR_{meas}, with a single-peak curve for parallel pump-polarization and a double-peak curve for perpendicular pump-polarization. The calculated ΔR_{def} and measured ΔR_{meas} roughly follow the same fluence dependence ($\Delta R_{\text{def}} \propto \Delta R_{\text{meas}}$). However, the calculated ΔR_{def} tends to underestimate the measured relative reflection changes as measured at ΔR_{meas}. This is because ΔR_{meas} contains both the increase in reflectivity caused by grating line deformation, and those caused by refractive index changes, whereas the calculations ignore the latter. The impact of the reflectivity changes on ΔR is evident from the positive measured ΔR_{meas} observed on flat silicon surfaces (see Fig. 3(a)). Comparing the AFM cross sections depicted in Fig. 8(c), the deformation sequence between ∥ and ⊥ pump polarization is indeed different. Especially around the double peak position (line 3 and 7), where, for ∥ polarization, the line and valley have the same shape, whereas for ⊥ polarization, only a small part of the line remains, and a steep slope at the inverted valleys is formed. When considering both probe polarizations, our calculations show that the double peak is absent for ∥ (Fig. 8(a)) but present for ⊥ (Fig. 8(b)) pump-polarization. Additionally, ⊥-polarized *probe* light enhances the sensitivity to the reflectivity change as induced by deformation. On top of this, the optical reflectivity shows reflection features, such as the double peak structure found in Fig. 8(b), which can only be attributed to grating line shape changes only. So next to changes in the complex refractive index, the reflectivity of gratings are also strongly affected by modification in the shape of the grating, resulting in, for example, a double peak structure in the reflectivity change as function of pump pulse fluence.

4. Conclusion

We investigated light-induced optical and topographical changes on flat silicon and silicon gratings exposed to single ultrafast laser pulses, with pump polarization parallel or perpendicular to the grating lines. For the gratings, additional thresholds for structural changes such as deformation, ablation, and crater formation were identified. The damage threshold fluences were found to be 10 to 50% lower for gratings than for flat silicon. Calculations suggest that localized field enhancements resulting from the grating topography significantly influence damage thresholds, indicating that localized effects, rather than total power absorption, determine damage thresholds. Using near-field RCWA, we calculated power density profiles to predict fluence thresholds, showing moderate correlation with experimental values. Hence, further model refinements are needed, such as the incorporation of heat diffusion [36], hydrodynamics, and nonlinear effects to make the model more quantitative. This should provide light-induced damage threshold (LIDT) value estimations for structured samples used in nanolithography, where alignment gratings are exposed to bright light sources. Our experiments show that the onset of optical changes coincides with the onset of grating line deformation, implying that the melting temperature is reached. This permanent material and optical change is unacceptable in the semiconductor device manufacturing. For flat silicon, the threshold for light-induced optical changes is ≈91 mJ/cm^2 for illumination with a single-shot 400 nm, 45 fs pulse. For the grating structures, this threshold can

reach values even below 40 mJ/cm^2, as measured on a 430 nm pitch, 23.2% duty-cycle grating. Since localized field enhancements significantly lower the damage thresholds, these numbers represent absolute upper limits for our grating-based alignment markers in Si. Note, however, that these fluences change when grating parameters are different, indicating that measurements of the light-induced damage fluence thresholds should be carried out when grating parameters change. On top of changes in the complex refractive index, we found that the enhanced relative reflection changes (ΔR) for gratings, with respect to those for flat silicon, were due to grating line deformation. In addition to the reported non-transient, permanent optical changes, and transient and recoverable changes that arise from the temporary heating of the electron gas can also be used. Although interpretation and translation of these optical responses into a clear warning threshold for permanent damage remains somewhat challenging, such measurements can still provide valuable insight into the heating process, even in regimes well below any critical temperatures when permanent damage occurs.

The onset of these deformations, resulting in optical changes, can serve as an early indicator of catastrophic failure. Our work provides the beginning of a framework for predicting and reducing light-induced damage in gratings by correlating grating pitch and duty-cycle with optical damage.

Disclosures. The authors have no conflicts to disclose.

Data availability. Data underlying the results presented in this paper may be obtained from the authors upon reasonable request.

Supplemental document. See Supplement 1 for supporting content.

References

1. S. Shead, "The Dutch firm that investors are going wild over is now creating a machine that could redefine electronics," (2021). [Accessed 28-06-2024].
2. G. Zhang, M. Graef, and F. van Roosmalen, "The rationale and paradigm of "more than Moore"," in *56th Electronic Components and Technology Conference* (2006), pp. 7.
3. M. M. Waldrop, "The chips are down for Moore's law," Nat. News **530**(7589), 144–147 (2016).
4. W. Rudolph, L. Emmert, Z. Sun, *et al.*, "Laser damage in dielectric films: What we know and what we don't," in *Laser-Induced Damage in Optical Materials*, vol. 8885, G. J. Exarhos, V. E. Gruzdev, J. A. Menapace, D. Ristau, and M. Soileau, eds., International Society for Optics and Photonics (SPIE, 2013), p. 888516.
5. M. Vreugdenhil and D. van Oosten, "Pulse duration dependence of single-shot pulsed laser ablation of gallium based III-V compound semiconductors," in *Laser-Induced Damage in Optical Materials*, vol. 12726, C. W. Carr, D. Ristau, C. S. Menoni, and M. D. Thomas, eds., International Society for Optics and Photonics (SPIE, 2023), p. 1272609.
6. E. Abram, I. Milov, N. Orlov, *et al.*, "Pre-ablation regime light-induced optical changes in nanometer thick metal films," Opt. Express **32**(3), 4564–4587 (2024).
7. J. R. Gulley, "Frequency dependence in the initiation of ultrafast laser-induced damage," in *Laser-Induced Damage in Optical Materials*, vol. 7842, G. J. Exarhos, V. E. Gruzdev, J. A. Menapace, D. Ristau, and M. J. Soileau, eds., International Society for Optics and Photonics (SPIE, 2010), p. 78420U.
8. M. Jupé, L. Jensen, K. Starke, *et al.*, "Analysis in wavelength dependence of electronic damage," in *Laser-Induced Damage in Optical Materials*, vol. 7504, G. J. Exarhos, V. E. Gruzdev, D. Ristau, M. J. Soileau, and C. J. Stolz, eds., International Society for Optics and Photonics (SPIE, 2009), p. 75040N.
9. L. Gallais, D.-B. Douti, M. Commandré, *et al.*, "Wavelength dependence of femtosecond laser-induced damage threshold of optical materials," J. Appl. Phys. **117**(22), 223103 (2015).
10. B. Rethfeld, K. Sokolowski-Tinten, D. Von Der Linde, *et al.*, "Timescales in the response of materials to femtosecond laser excitation," Appl. Phys. A **79**(4-6), 767–769 (2004).
11. M. F. Koldunov, A. A. Manenkov, and I. L. Pokotilo, "Mechanical damage in transparent solids caused by laser pulses of different durations," Quantum Electron. **32**(4), 335–340 (2002).
12. J.-Y. Natoli, L. Gallais, H. Akhouayri, *et al.*, "Laser-induced damage of materials in bulk, thin-film, and liquid forms," Appl. Opt. **41**(16), 3156–3166 (2002).
13. A. A. Manenkov and A. M. Prokhorov, "Laser-induced damage in solids," Sov. Phys. Usp. **29**(1), 104–122 (1986).
14. Y. Li, Z. Yuan, J. Wang, *et al.*, "Laser-induced damage characteristics in fused silica surface due to mechanical and chemical defects during manufacturing processes," Opt. & Laser Technol. **91**, 149–158 (2017).

15. J. Xu, L. Lin, J. Ji, *et al.*, "Controlled plasmonic nanowelding of metal nanoparticles under ultrafast laser irradiation for printable nanocircuits," ACS Appl. Nano Mater. **7**(5), 4824–4834 (2024).

16. A. Schirato, M. Maiuri, G. Cerullo, *et al.*, "Ultrafast hot electron dynamics in plasmonic nanostructures: experiments, modelling, design," Nanophotonics **12**(1), 1–28 (2023).

17. E. Abram, N. Orlov, E. C. Garnett, *et al.*, "Sub-ablation-threshold light-induced modification of thin ruthenium layers detected using optical reflectance," J. Appl. Phys. **136**(24), 245305 (2024).

18. M. van Kraaij, "Forward diffraction modelling: analysis and application to grating reconstruction," (2011).

19. R. van Haren, S. Steinert, O. Mouraille, *et al.*, "Intra-field mask-to-mask overlay, separating the mask writing from the dynamic pellicle contribution," in *Photomask Japan: XXV Symposium on Photomask and Next-Generation Lithography Mask Technology*, vol. 10807, K. Takehisa, ed., International Society for Optics and Photonics (SPIE, 2018), p. 108070K.

20. E. D. Palik, *Handbook of Optical Constants of Solids*, vol. 3 (Academic Press, 1998).

21. C. Herzinger, B. Johs, W. McGahan, *et al.*, "Ellipsometric determination of optical constants for silicon and thermally grown silicon dioxide via a multi-sample, multi-wavelength, multi-angle investigation," J. Appl. Phys. **83**(6), 3323–3336 (1998).

22. W. M. Haynes, *CRC Handbook of Chemistry and Physics* (CRC Press, 2014), 95th ed.

23. Itseez, "Open source computer vision library," https://github.com/itseez/opencv (2024).

24. M. A. Fischler and R. C. Bolles, "Random sample consensus: a paradigm for model fitting with applications to image analysis and automated cartography," Commun. ACM **24**(6), 381–395 (1981).

25. F. Schwidefsky, "Increase of the refractive index of silicon films by dangling bonds," Thin Solid Films **18**(1), 45–52 (1973).

26. S. Chandrasekhar, A. Vengurlekar, V. Karulkar, *et al.*, "Temperature, light intensity and microstructure dependence of the refractive index of polycrystalline silicon films," Thin Solid Films **169**(2), 205–212 (1989).

27. M. Janai, D. Allred, D. Booth, *et al.*, "Optical properties and structure of amorphous silicon films prepared by cvd," Sol. Energy Mater. **1**(1-2), 11–27 (1979).

28. D. Aspnes, "Optical properties of thin films," Thin Solid Films **89**(3), 249–262 (1982).

29. Y. Liu, Y. Ding, J. Xie, *et al.*, "One-step femtosecond laser irradiation of single-crystal silicon: Evolution of micro-nano structures and damage investigation," Mater. & Design **225**, 111443 (2023).

30. L. Cruciani, M. Vreugdenhil, S. van Vliet, *et al.*, "Direct laser patterning of ruthenium below the optical diffraction limit," Appl. Phys. Lett. **124**(17), 171902 (2024).

31. "Microscope-based Film Thickness Measurement Instrument - Filmetrics F40," https://www.kla.com/products/instruments/thin-film-reflectometers/filmetrics-f40. [Accessed 15-05-2025].

32. T. Paschen, R. Roussel, L. Seiffert, *et al.*, "Ultrafast strong-field electron emission and collective effects at a one-dimensional nanostructure," ACS Photonics **10**(2), 447–455 (2023).

33. H. Zhang, S. A. Wolbers, D. M. Krol, *et al.*, "Modeling and experiments of self-reflectivity under femtosecond ablation conditions," J. Opt. Soc. Am. B **32**(4), 606–616 (2015).

34. M. E. Povarnitsyn, T. E. Itina, M. Sentis, *et al.*, "Material decomposition mechanisms in femtosecond laser interactions with metals," Phys. Rev. B **75**(23), 235414 (2007).

35. D. S. Ivanov and L. V. Zhigilei, "Combined atomistic-continuum modeling of short-pulse laser melting and disintegration of metal films," Phys. Rev. B **68**(6), 064114 (2003).

36. J.-F. Bryche, M. Vega, J. Moreau, *et al.*, "Ultrafast heat transfer at the nanoscale: Controlling heat anisotropy," ACS Photonics **10**(10), 1177–1186 (2023).

37. D. Necas and P. Klapetek, "Gwyddion: an open-source software for SPM data analysis," Cent. Eur. J. Phys. **10**, 181–188 (2012).